ISSN 0015-4628, Fluid Dynamics, 2019, Vol. 54, no. 5, pp. 724–738. © Pleiades Publishing, Ltd., 2019.
Russian Text © The Author(s), 2019, published in Izvestiya RAN. Mekhanika Zhidkosti i Gaza, 2019, No. 5, pp. 135–149.

Flow Characteristics of a Supersonic Open Cavity

J. M. Wang[a,*], X. J. Ming[a,b], H. Wang[a], Y. Ma[a], and J. Q. Wu[c,]**

[a] *Liaoning Key Lab of Advanced Test Technology for Aerospace Propulsion, Shenyang Aerospace University, Shenyang, 110136 China*

[b] *Sichuan Aerospace Zhongtian Power Equipment Co., Ltd, Chengdu, 610100 China*

[c] *China Aerodynamics Research and Development Center, Mianyang, 621000 China*

**e-mail: jmwang_sau@163.com*

***e-mail: junqiangwu_cardc@163.com*

Received May 8, 2018; revised November 12, 2018; accepted February 10, 2019

Abstract—An open cavity flow exhibits intense self-sustained oscillations. This transient behavior stimulates violent pressure fluctuations because of multiple-order cavity tones. Detached eddy simulation was conducted to simulate the cavity flow at the freestream Mach number of 1.19. In order to improve the understanding of the shear layer convection processes and frequency characteristics the velocity of the flow field at cavity mid-span was studied using the dynamic mode decomposition (DMD) algorithm. The first three modes of the supersonic cavity flow were extracted to describe the flow configuration at the dominant frequencies. The two-vortices, three-vortices, and four-vortices are the corresponding first three DMD modes. The simplified mode structures are proposed to explain the flow dynamics in a supersonic cavity. When a feedback compression wave encounters the extrusion wave at a special location, an "analogous sonic boom" phenomenon appears causing violent noise in the cavity.

Keywords: supersonic flow, cavity flows, clear weapon bay, dynamic mode decomposition

DOI: 10.1134/S0015462819050124

Cavity flows arise in many aerospace applications, such as wheel wells, weapon bays, and other fuselage openings for telescopes and sensors [1]. Since the 1950s, the similar cavity flow has been examined by numerous researchers all over the world. A large number of earlier researches were conducted by Rossiter and Roshko, through a theoretical analysis and experimental observations [2]. By examining the shadowgraph pictures along with the data from pressure sensors, Rossiter first put forward the linear theoretical model of the cavity flow. His famous semi-empirical frequency prediction formula is as follows:

$$\frac{fl}{U} = \frac{m - \alpha}{\mathrm{Ma} + 1/k}. \tag{0.1}$$

Equation (0.1) is based on the convection velocity of the shear layer, the frequency of the shedding vortices, and the speed of the feedback acoustic wave [3]. Here, f is the frequency, l is the length of the cavity, k is the vortex convection speed divided by the freestream speed U, Ma is the freestream Mach number, α is a constant, and $m = 1, 2, 3, \ldots$. Here, α is equal to 0.25 and k is equal to 0.57 [3]. At low Mach numbers this assumption introduces only a small error but at high Mach numbers the error is much greater. The modified Heller formula (0.2) considerably improves the correlation at high Mach numbers assuming that the cavity sound speed is equal to the freestream stagnation sound speed. The formula for the Strouhal number is as follows:

$$\frac{fl}{U} = (m - \alpha) \Bigg/ \left\{ \frac{\mathrm{Ma}}{\left[1 + (\gamma - 1)\mathrm{Ma}^2/2\right]^{1/2}} + \frac{1}{k} \right\}. \tag{0.2}$$

Tam and Block settled up a mathematical model of cavity tones and pressure oscillation phenomenon, which is based on the coupling between shear layer instabilities and the acoustic feedback [3]. Zhuang et al. (2006) found five different waves by examining the shadowgraph photographs of cavity flow [4], which were confirmed by Moon et al. (2010) through the high speed schlieren [5]. Schmit et al. (2011)

found the entrainment wave by examining the flow shadowgraphs and indicated that the cavity tones are excited by the entrainment waves impacting the rear wall rather than by the shedding vortices which cause the broad bandnoise [6]. Moreover, Wang et al. (2017) investigated the entrainment characteristics of cavity shear layers in supersonic flows and proposed that entrainment of the freestream fluid into the cavity recirculation zone is produced by the interaction between the shear layer and the cavity aft wall [7]. Currently, there are various interpretations of the flow mechanism about the cavity; it still not comes to an agreement. The frequencies of the cavity tones can be predicted by the Rossiter and Heller formulas but the choice of empirical parameters is not general [8].

At high freestream Mach numbers, the sound pressure level of cavity tones can reach 170 dB, corresponding to r.m.s pressure amplitudes of 6300 Pa [1]. Not only the amplitudes are large but also the pressure waves are spatially correlated, which quickly leads to structural fatigue issues inside the aircraft. Analyzing the coherent structures with different orders will help us to put forward methods, which cut off some or other steps of the feedback loop more targeted and to develop the more effective active-passive control technology [9]. Neither the sound pressure level (SPL) with different orders nor the distribution of the SPL at different freestream Mach numbers is same in the cavity flow. The competitive relation of the energy with different orders is existent [10].

In order to understand the underlying physical mechanism of the cavity tones, the coherent structures with different frequencies must be extracted. The common technique for identifying the coherent structures is the proper orthogonal decomposition (POD) [11]. However two major drawbacks, which are tactically acknowledged in employing this method, are associated with this technique. Firstly, the energy can be the incorrect measure to rank the flow structures in all circumstances. Secondly, due to the choice of the second-order statistics as the basis for the decomposition, valuable phase information is lost [12]. However, dynamic mode decomposition (DMD) is suitable for analyzing the flow dynamics around the cavity. The DMD approach was first proposed by Schmid and Sesterhenn in 2008 and later published in [12]. DMD is a recent technique decomposing a dynamical system into the modes based on the Koopman analysis, thus making it possible to extract latent physical mechanisms. DMD is an effective method, as applied to experimental and numerical flow field data. A low-dimensional matrix constitutes the coherent dynamics of the temporal-spatial field. The Ritz eigenvalues and eigenvectors of the low-dimensional matrix capture the latent dynamics of a dynamical system. The method has been applied to various complex dynamics, such as jets in different cases [13], thermo-acoustic unstable systems [14], wake flows [15], and turbulent cavity flows [16]. Furthermore, several decomposition techniques of similar fashion were developed based on the standard DMD algorithm, such as the optimal mode decomposition [17], the sparsity-promoting DMD [18], the total DMD [19], and other modified methods. The developed methods can more accurately extract the modes and expand the applications of the DMD algorithm. In order to highlight the variation of the dynamics, in this paper the modes extracted with the DMD algorithm are evolutive in the time domain.

Several important aspects (such as the interaction of the feedback wave and the shear layer) of supersonic open cavity flows still need to be fully understood and entirely explored. Detached eddy simulations (DES) were conducted to simulate a supersonic cavity flow. The multiple-frequency phenomena and the oscillation of supersonic cavity flow were studied in this paper. The flow structures at cavity mid-span were studied by the DMD algorithm. Moreover, the dominant modes were extracted to reveal the underlying oscillations. The simplified mode structures of the cavity dynamics were obtained.

1. DYNAMIC MODE DECOMPOSITION

The cavity flow contains a variety of flow phenomena, including shock waves, compression waves, unstable shear layers, and dynamics of vortices. These phenomena involve multiple flows with the interaction between different frequencies. DMD provides an ability to extract the coherent structures with different frequencies.

The temporal-spatial field of a transient flow can be expressed by a matrix $V_1^N = [v_1, v_2, \ldots, v_i, \ldots, v_{N-1}, v_N]$, where the vector v_i is the spatial distribution of the flow parameters on temporal slice i (Fig. 1).

The time step between two neighboring columns is Δt. When the sampling time is adequate, DMD assumes that the evolution from v_i to v_{i+1} is generated by an approximated linear dynamical system of the form:

$$v_{i+1} = Av_i. \tag{1.1}$$

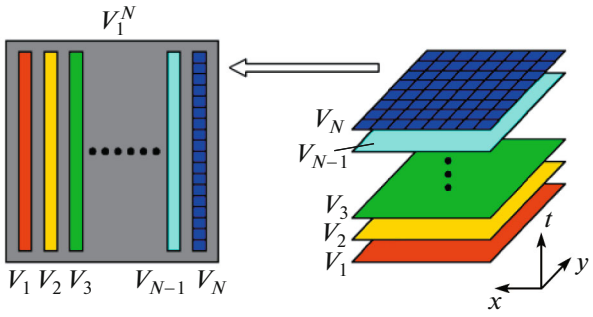

Fig. 1. Formation of the temporal-spatial matrix.

Since the vectors given by Eq. (1.1) are linearly dependent, the last vector V_N can be expressed in terms of the previous vectors as follows:

$$v_N \approx V_1^{N-1} c \tag{1.2}$$

with the coefficients $c^T = \{c_1, c_2, \cdots, c_{N-1}\}$. Following the Arnoldi algorithm, the linear matrix A can be written in the form:

$$A\{v_1, v_2, \cdots, v_{N-1}\} = \{v_2, v_3, \cdots, v_N\} \approx \{v_2, v_3, \cdots, v_{N-1} c\}. \tag{1.3}$$

Equation (1.3) can be written in the form:

$$A V_1^{N-1} = V_2^N \approx V_1^{N-1} K, \tag{1.4}$$

where K is the companion matrix of the system matrix A.

Using the least squares method we can recover the companion matrix K in the form of the following expression

$$K = \begin{pmatrix} 0 & & & c_1 \\ 1 & 0 & & c_2 \\ & \mathrm{O} & \mathrm{O} & \mathrm{M} \\ & & 1 & 0 \; c_{N-2} \\ & & & 1 \; c_{N-1} \end{pmatrix}. \tag{1.5}$$

The coefficients can be obtained according to the formula

$$c = W \Sigma^{-1} U^H v_N \tag{1.6}$$

with $V_1^{N-1} = U \Sigma^{-1} W^H$ determined by singular value decomposition (SVD).

The Ritz eigenvalues λ_i of K approximate some of the Ritz eigenvalues of A. The Ritz eigenvalues of the companion matrix K are logarithmically mapped onto the complex plane, where their real parts represent the exponential growth or decay, while their imaginary parts contain the temporal frequency. The dynamic mode of DMD may be obtained by the following function

$$\Phi_i = U y_i, \tag{1.7}$$

where y_i is the ith eigenvector of K and U are the right singular vectors of the snapshot sequence V_1^{N-1}; Φ_i is also the corresponding dynamical mode of DMD. The extracted dynamic modes may be used to provide the coherent dynamics information and each mode has a single distinct frequency. More detailed description of the DMD algorithm can be found in [12].

2. NUMERICAL SIMULATION AND VALIDATIONS

2.1. Governing Equations and Algorithm

In the present study the Navier—Stokes equations were used to calculate the unsteady viscous flow. The governing equations are as follows:

continuity equation

$$\frac{\partial \rho}{\partial t} + \nabla \bullet (\rho \overset{\mathrm{r}}{\mathbf{v}}) = 0\,; \tag{2.1}$$

momentum equation

$$\frac{\partial}{\partial t}(\rho \overset{\mathrm{r}}{\mathbf{v}}) + \nabla \bullet (\rho \overset{\mathrm{rr}}{\mathbf{vv}}) = -\nabla p + \nabla \bullet \overline{\overline{\tau}}, \tag{2.2}$$

where p is the static pressure. The stress tensor $\overline{\overline{\tau}}$ is given by the expression

$$\overline{\overline{\tau}} = \mu\left[(\nabla \overset{\mathrm{r}}{\mathbf{v}} + \nabla \overset{\mathrm{r}}{\mathbf{v}}^{T}) - \frac{2}{3}\nabla \bullet \overset{\mathrm{r}}{\mathbf{v}}\mathrm{I}\right], \tag{2.3}$$

where μ is the turbulent viscosity and I is the unit tensor.

Energy equation

$$\frac{\partial}{\partial t}(\rho E) + \nabla \cdot (\overset{\mathrm{r}}{\mathbf{v}}(\rho E + p)) = \nabla \cdot \left(k_{\mathrm{eff}} \nabla T - \sum_{j} h_j \overset{\mathrm{r}}{\mathbf{J}}_j + (\overline{\overline{\tau}}_{\mathrm{eff}} \cdot \overset{\mathrm{r}}{\mathbf{v}})\right), \tag{2.4}$$

where k_{eff} is the effective thermal conductivity and E is the total energy. The first three terms on the right-hand side of Eq. (2.4) represent the energy transfer due to heat conduction, species diffusion, and viscous dissipation, respectively.

The simulation was conducted using DES based on the SST k–ω turbulence model described in [20]. The kinetic energy of turbulence κ and the specific dissipation rate ω are obtained from the following transport equations

$$\frac{\partial}{\partial t}(\rho\kappa) + \frac{\partial}{\partial t}(\rho\kappa u_i) = \frac{\partial}{\partial x_j}\left[\Gamma_k \frac{\partial \kappa}{\partial x_j}\right] + G_k - Y_k, \tag{2.5}$$

$$\frac{\partial}{\partial t}(\rho\omega) + \frac{\partial}{\partial t}(\rho\omega u_i) = \frac{\partial}{\partial x_j}\left[\Gamma_\omega \frac{\partial \omega}{\partial x_j}\right] + G_\omega + D_\omega - Y_\omega. \tag{2.6}$$

In these equations G_k determines the generation of the turbulent kinetic energy due to mean velocity gradients and G_ω determines the generation of ω. The quantities Γ_k and Γ_ω represent the effective diffusivities of k and ω, respectively, while Y_k and Y_ω represent the dissipation of k and ω due to turbulence. Finally, D_ω is the cross-diffusion term. The expression for the dissipation of k can be written in the form:

$$Y_k = \rho\beta^* k\omega F_{\mathrm{DES}}, \tag{2.7}$$

where β^* is a constant of the model, while the expression for F_{DDES} is as follows:

$$F_{\mathrm{DDES}} = \tanh[(C_{d1} r_{d1})^{C_{d2}}], \tag{2.8}$$

where $C_{d1} = 20$, $C_{d2} = 3$, and

$$r_d = \frac{\nu_t + \nu}{\kappa^2 y^2 \sqrt{0.5 g(S^2 + \Omega^2)}}. \tag{2.9}$$

Here, S is the magnitude of the strain rate tensor and Ω is the magnitude of the vorticity tensor. In more detail the numerical model is described in [20].

2.2. Computational Parameters

The simulation was conducted under the same flow conditions as in Hamed's investigation [20]. The commercial software ANSYS/Fluent was used to simulate the open cavity flow. The freestream Mach number was 1.19. The delayed DES/SST turbulence model was chosen, similar but not identical with [22]. Figure 2 displays the schematic representation of the cavity configuration, where the length to depth ratio $l/d = 5$. The grid was refined near the walls with a minimum grid spacing of $1 \times 10^{-3}D$, while the maximum value $y^+ < 4$ was taken in the outlet region and 15 grid points were taken within the $0.1D$ boundary layer thickness at the upstream cavity lip. The computational grid conforms to the requirement of DES. The freestream conditions were set for the supersonic inflow and the periodic boundary conditions were

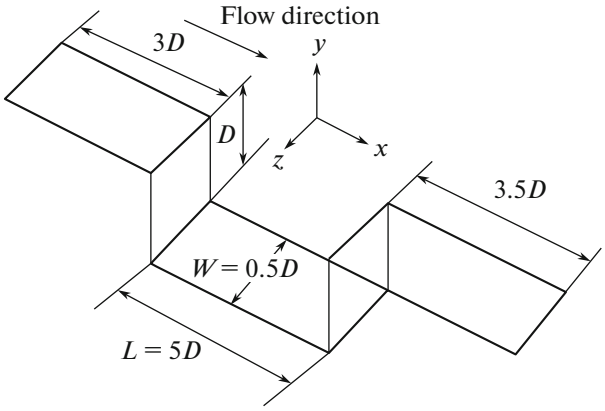

Fig. 2. Schematic representation of the cavity configuration.

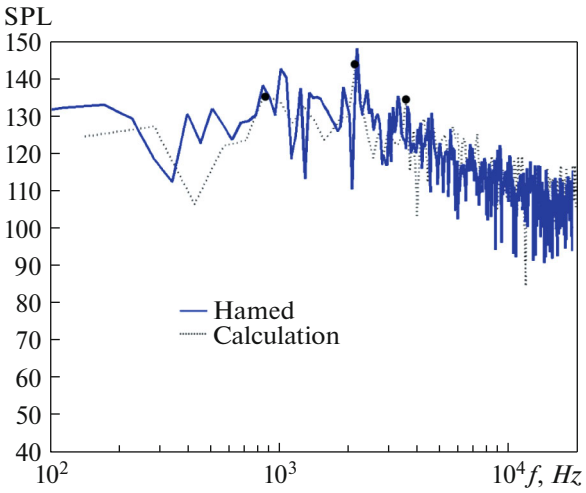

Fig. 3. Comparison of the calculated SPL spectra with Hamed's results [21] near the rear wall.

applied in the spanwise direction. The pressure fluctuations at 39 equidistant points (Point01 at $x = 0.025L$, consecutively numbered to Point39 at $x = 0.975L$) were sampled on the cavity ceiling of the symmetry plane uniformly. In order to capture the frequency fluctuations of the cavity flow, the time step was 10^{-6} s and the temporal span of the simulation was greater than 20 times the period of the first-order cavity tone, which is predicted by Heller's formula.

2.3. Validations of the Simulation Results

As can be seen in Fig. 3, the results of the calculations agree with Hamed's data [21]; here, f is the pressure fluctuation frequency. The first three cavity tone modes (plotted by the dots in Fig. 3) have the higher sound pressure level. The second cavity tone is the loudest in the cavity (same as the results of [23]).

The overall sound pressure level (OASPL) can be written as follows:

$$\mathrm{OASPL} = 20 \log \frac{P_{\mathrm{rms}}}{P_{\mathrm{ref}}}, \tag{2.10}$$

where P_{rms} is the r.m.s. of the pressure oscillations with respect to the mean ambient pressure and $P_{\mathrm{ref}} = 20\ \mu\mathrm{Pa}$.

Table 1. Comparisons of the Strouhal numbers at Mach 1.19

Mode	1	2	3
Heller's formula	0.2674	0.6239	0.9804
Hamed's results	0.2860	0.6238	0.9394
SPL of the DES results	0.2464	0.6240	1.0017

The dimensionless Strouhal number is defined as $St = fl/U$. Table 1 gives the Strouhal numbers of the cavity peak frequencies at Mach 1.19 in comparison with Heller's formula and Hamed's results [21]. As shown in Table 1, the calculated results of this study almost match the frequencies estimated by Heller's formula and Hamed's results. Figure 4 compares the *OASPL* on the cavity ceiling with Hamed's results and the experimental results [6]. The figure shows that the results calculated in this study predict the general rise in *OASPL* toward the rear end wall. Based on the comparisons, the data calculated in this study are reliable to analyze the dynamical system.

3. RESULTS AND ANALYSIS

3.1. The Three-Dimensional Coherent Dynamics

To identify the three-dimensional coherent dynamics of the cavity flow Fig. 5 illustrates the instantaneous snapshots of the three-dimensional flow structures visualized by means of the dimensionless Q criterion, where Q is defined as follows:

$$Q = \frac{1}{2}(\|\Omega\|^2 - \|S\|^2), \tag{3.1}$$

where $\|\bullet\|$ is the Euclidean matrix norm, S is the magnitude of the strain rate tensor, and Ω is the magnitude of the vorticity tensor [24]. The regions, where $Q > 0$ (colored by red), are occupied by vortical structures.

As can be seen in Fig. 5, complex vortex structures dominate the flow field inside the cavity. The instability of the shear layer is strengthened and the vortices are produced, as the shear layer passes the leading edge of the cavity. As the vortices move downstream, the size of the vortices becomes greater. The shear layer is divided into two parts by the trailing edge. One part enters the cavity and the other moves downstream.

3.2. Flow Structures at Cavity Mid-Span

Figure 6 shows the instantaneous snapshots of the flow structures at cavity mid-span in the form of streamlines and contours of the Mach number, Cp, and $\partial P/\partial x$. Each phase in Fig. 6 is consistent with the

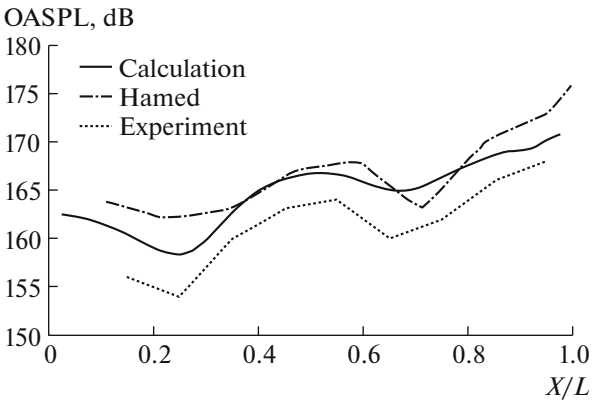

Fig. 4. Variation of *OASPL* on the cavity ceiling.

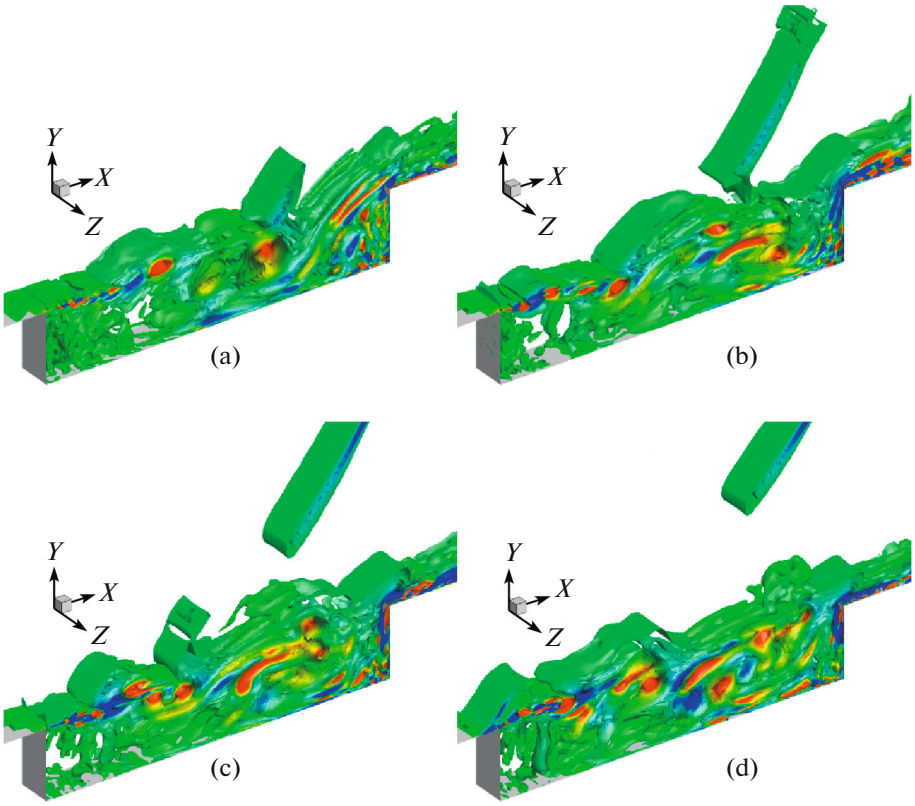

Fig. 5. Instantaneous snapshots of the three-dimensional flow structures visualized by the Q criterion.

corresponding phase in Fig. 5. The pressure coefficient is defined as $Cp = \dfrac{P - P_\infty}{1/2\,\rho U_\infty^2}$. Figure 6d shows the contours of the pressure gradient $\partial P/\partial x$, where the red regions represent the compression waves and the blue ones represent the expansion waves.

Due to the freestream driving effect, the shear layer passes the leading edge of the cavity and a vortex forms and starts to translate downstream. It gains enough rotational momentum to carry a small portion of the freestream flow into the cavity (as seen in Fig. 6a). With the impingement of the shear layer (entrainment wave, actually, [6]) on the rear wall, a local high pressure area (as seen in Fig. 6c), a reflected acoustic wave (compression wave), and a shock wave are formed near the trailing edge (as can be seen in Fig. 6d). The reflected acoustic wave travels upstream along the ceiling of the cavity. Because of the stimulation of the reflected acoustic wave, the shear layer fluctuations are intensified in the direction of the cavity depth. The fluctuations of the shear layer are clearly visible Figs. 6a and 6b. When the acoustic wave arrives at the front wall of the cavity, a perturbation from the traveling acoustic wave disturbs the shear layer and a new vortex is formed near the leading edge of the cavity, so the next loop process begins. The similar phenomenon was observed in [25]. Moreover, the compression wave (seen in Fig. 6d (4)) and the expansion wave (Fig. 6d (2)) are alternately generated near the leading edge of the cavity [26].

Because the feedback acoustic wave is weak, it is clear that it can be identified with the contour of pressure gradient (as seen in Fig. 6d). It is worth to mention that there are several traveling feedback acoustic waves in the cavity (as seen in Fig. 6d); they were pointed out by Schmit et al. [6] by shadowgraph images. Meanwhile, the oblique shock waves are formed somewhere outside of the shear layer (as seen in Fig. 6b). It is necessary to point out that this feedback acoustic wave exists always but the shock waves stimulated by the acoustic wave are discontinuous. As can be seen in Fig. 6d (3), the front acoustic wave connects with the shock wave outside of the shear layer, while the rear one does not. Only if the acoustic wave travels to the special location, the shock waves can be stimulated. When the shock wave forms (as shown in Fig. 6d (3), the feedback acoustic wave connects with the oblique shock wave sometime. The phenomenon can be verified by the shadowgraph taken by Schmit et al. [6].

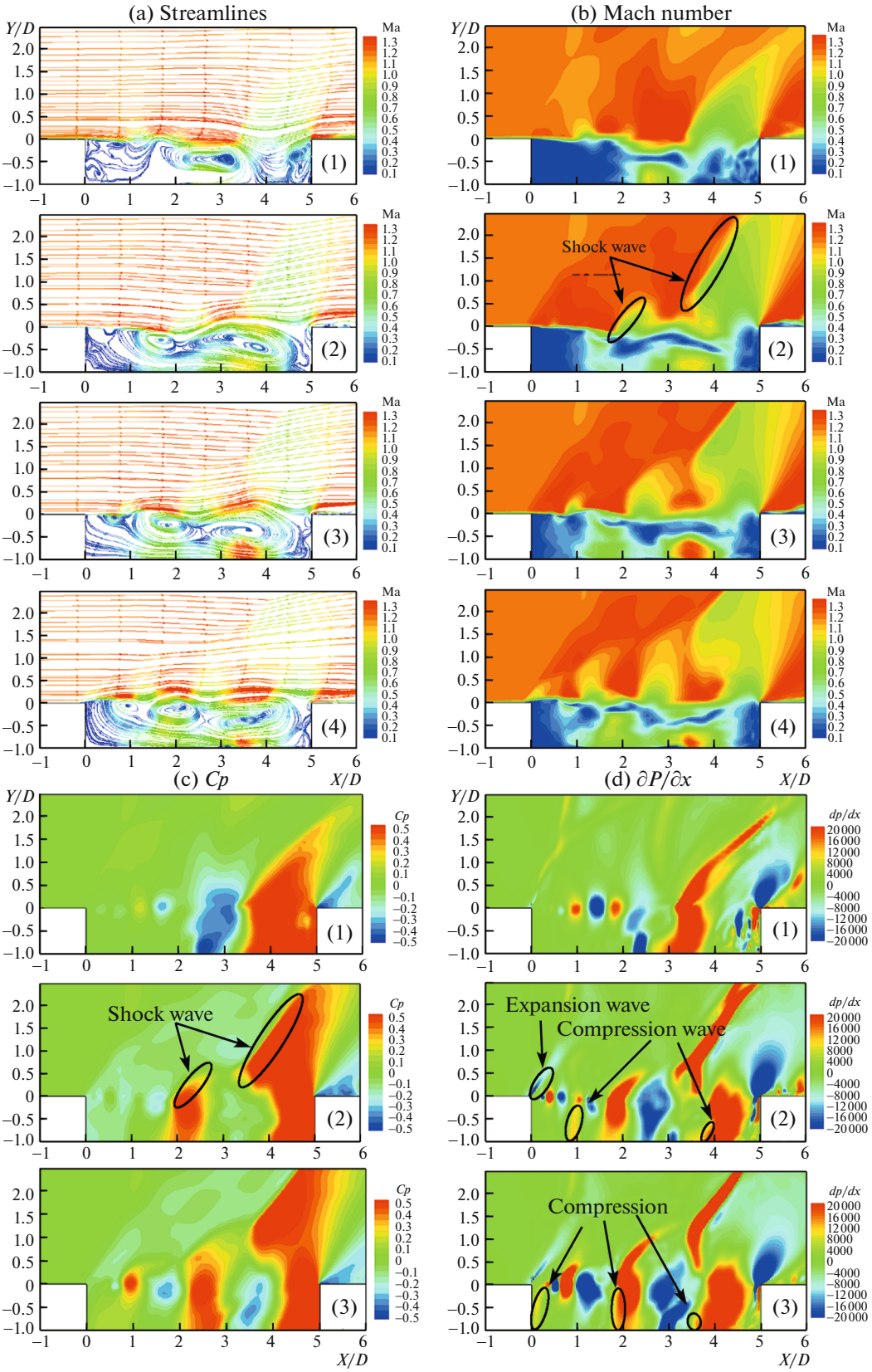

Fig. 6. Instantaneous snapshots of the flow structures at cavity mid-span.

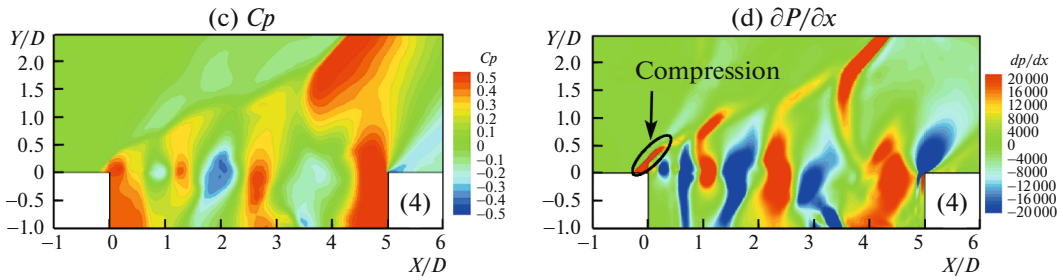

Fig. 6. (Contd.)

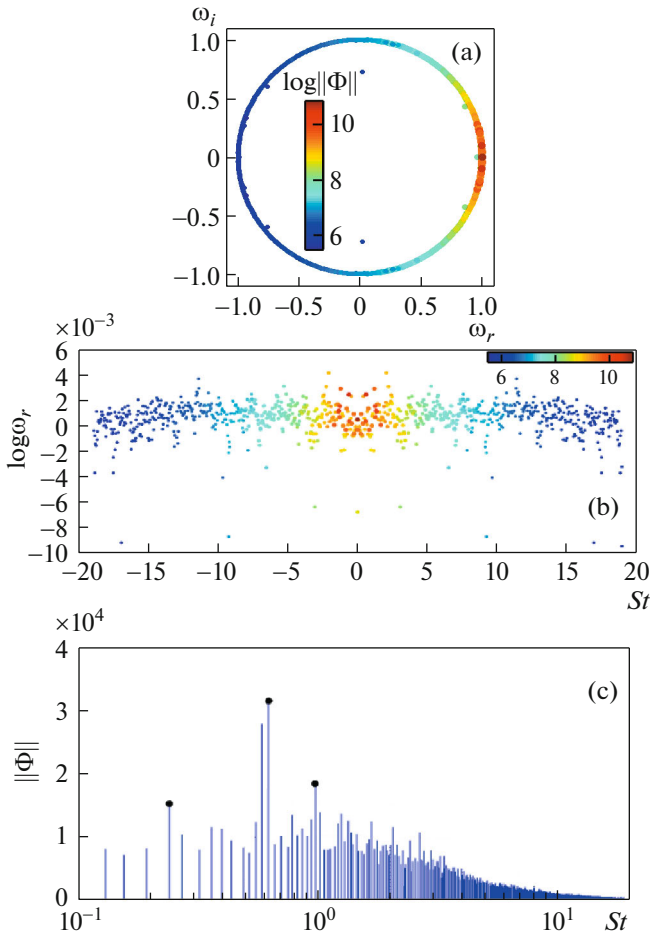

Fig. 7. Dynamic eigenvalue characteristics

4. THE DMD ANALYSIS OF THE VELOCITY FIELD AT CAVITY MID-SPAN

4.1. DMD Spectrum

Figure 7 presents the eigenvalue distribution of the companion matrix K. The colors of the scattered dots indicate the amplitudes $\log\|\Phi\|$ of the respective modes in the data sequence. It is distinct from Fig. 7a that most of the dynamic modes lie on or near the unit circle in the complex plane of λ_i, with the exception of only a few modes located inside the unit circle. It is suggested by the scattered dots that most modes are quasi-neutral and stable on the time dimension [19].

The natural logarithm of eigenvalue takes the form:

Table 2. Comparisons of the Strouhal numbers at Mach 1.19

Mode	1	2	3
Heller's formula	0.2674	0.6239	0.9804
SPL of the test data	0.2464	0.6240	1.0017
DMD analyses	0.2392	0.6218	0.9878

$$\log(\lambda_j)/\Delta t = \omega_j = \omega_r^{(j)} + \omega_i^{(j)}. \quad (4.1)$$

The imaginary part of ω_j, which represents the phase speed, contains the frequency information of the corresponding mode. The real part of ω_j indicates the perturbation growth or decay. In Fig. 7b a large proportion of the points lie around the zero line also indicating that the mode possesses the neutral stability on the time dimension. The abscissa $\omega_i^{(j)}/(2\pi)$ represents the frequency of the corresponding mode.

Each DMD mode is shown at its corresponding frequency in Fig. 7c, where f is the frequency and $\|\Phi\|$ represents the global energy norm of each mode. As the Ritz eigenvalues appear in complex conjugate pairs, only the modes with $f > 0$ are shown and the mean flow mode at $f = 0$ is not displayed in Fig. 7c. The tendencies of DMD analysis and SPL analysis are quite similar in amplitude, whereas they are rarely matched at frequency.

Table 2 displays the comparisons of the Strouhal numbers at Mach 1.19. The three frequencies based on the DMD almost match the peak frequencies estimated by Heller's formula and captured by the SPL spectrum.

4.2. The Extracted DMD Mode

Figure 8 shows the velocity vectors of the 0-mode calculated by the DMD algorithm, called the mean flow mode, which is unique and captures the time-mean flow structure. The velocity vectors are colored according to the velocity magnitude ($V_m = (u^2 + v^2 + w^2)^{0.5}$). It is clearly visible that the disturbance of the strong shear layer is located near the face of the cavity. As a result of shear layer separation, a smaller induced vortex near the leading edge rotates counterclockwise, whereas the dominant vortex, which occupies the main region of the cavity, rotates clockwise.

According to the evolution equation mentioned by Rowley et al. (2009), it is evident that the extracted dynamic modes can be evolutive at $\phi_i^m = \lambda_i^{m-1}\phi_i$, where ϕ_i^m is the phase of the dynamic mode and λ_i is the eigenvalue corresponding to the extracted dynamic mode.

Figure 9 shows the velocity vectors of the time-evolutive DMD modes. Every DMD mode is time-evolutive, so four phases are chosen for every mode. The actual cavity flow is the superposition of all the DMD modes. The vector arrows of velocity indicate the direction of flow oscillations. The Strouhal numbers corresponding to the dominant frequency of three DMD modes are 0.2392, 0.6218, and 0.9878, respectively (as seen in Table 2). In Fig. 9 the obvious distinctions of the first three different modes are the number of vortices and the vibration way of the shear layer. The 1st mode has a 2-vortex structure, the 2nd

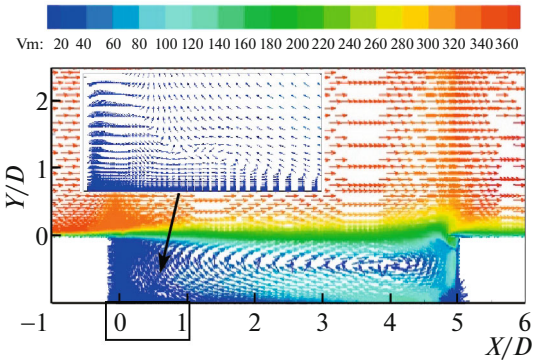

Fig. 8. Velocity vectors of the mean flow mode.

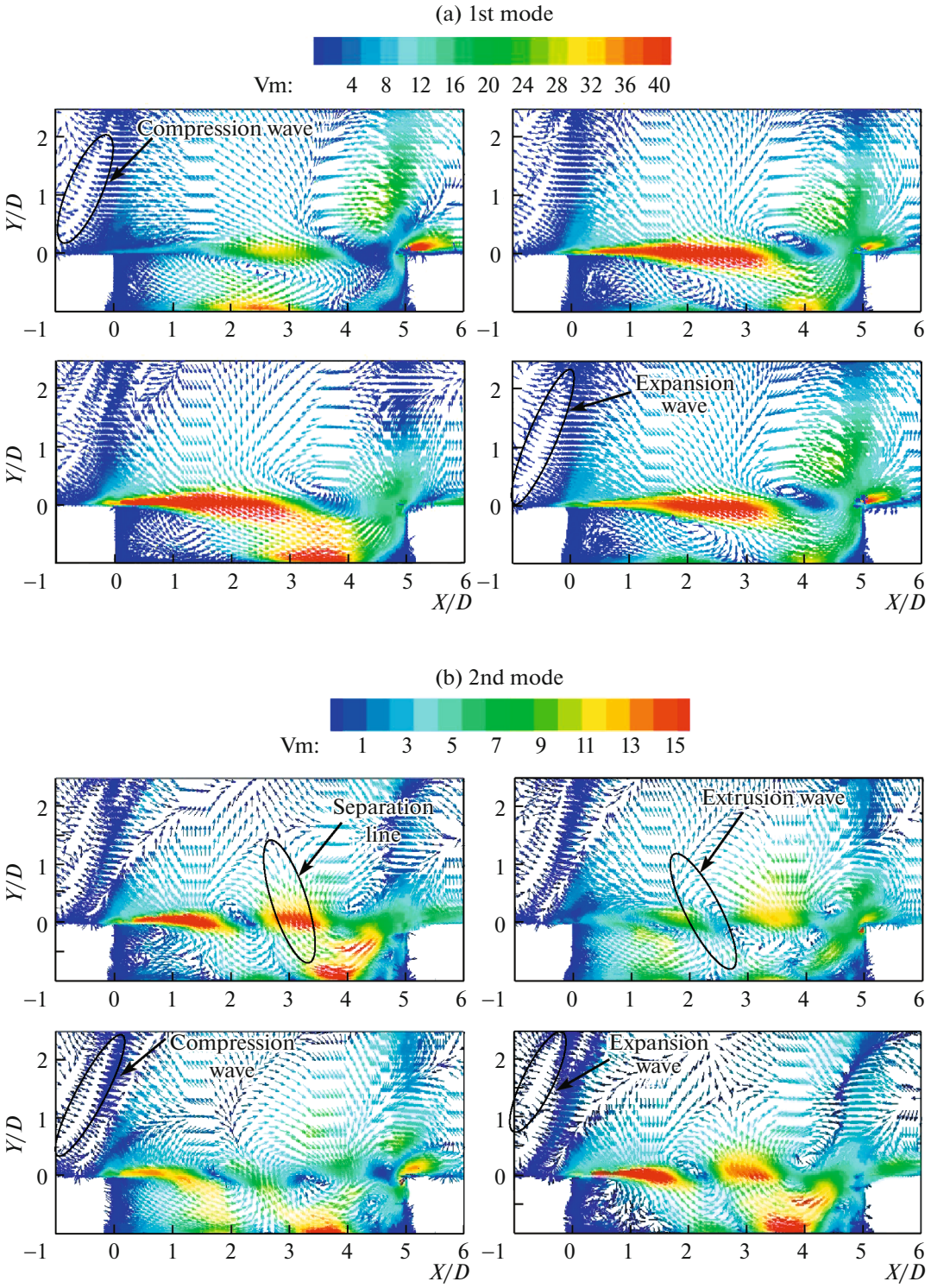

Fig. 9. Velocity vectors of the extracted DMD modes.

mode has a 3-vortex structure, and the 3rd mode has a 4-vortex structure. As the modes are evolutive in Fig. 9, the vortices are formed near the leading edge of the cavity and then travel downstream. The traveling vortex grows up in size and gradually rises inside the cavity. The vortex is extruded outside of the cavity near the rear wall and moves downstream.

As can be seen in Fig. 9, the compression wave and the expansion wave generate near the leading edge of the cavity, alternately. Heller and Delfs elaborated the phenomenon in detail in [26]. Furthermore, the

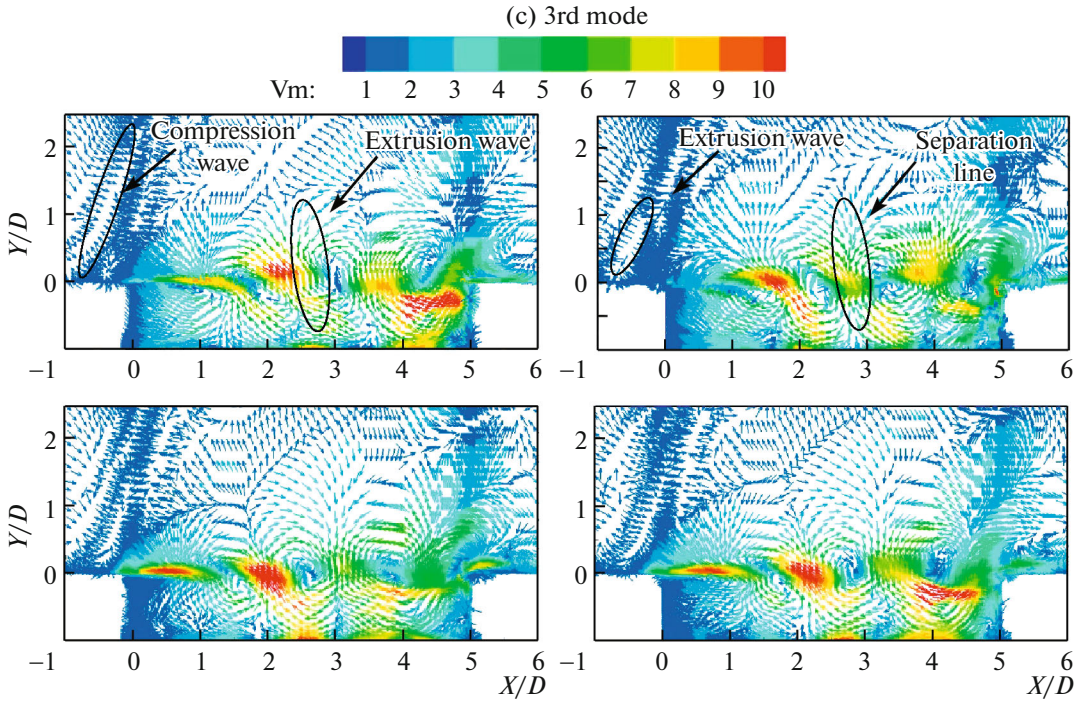

Fig. 9. (Contd.)

vortices are periodically connected by the extrusion wave or the separation line in different phase positions. When the adjacent vortices are extruded, there is an extrusion wave between them. The extrusion wave acts like a compression wave. Along the extrusion wave, the fluid enters into the freestream field from the cavity. When the adjacent vortices are away from each other, there is a separation line between them. The separation acts like an expansion wave. The fluid in the freestream enters into the cavity along the separation line. The extrusion wave and separation line translate downstream.

5. SIMPLIFIED MODE STRUCTURES OF THE OPEN CAVITY DYNAMICS

Based on the above discussion, Fig. 10 shows the simplified DMD mode structures of the cavity flow dynamics. Two typical phases of the previous every mode are displayed in Fig. 10. The colorized lines in Fig. 10 aim to distinguish different flow structures.

As shown in Fig. 10a, the major 2-vortex structure is characteristic of the 1st mode. The mode is time-evolutionary along different phases. With the impingement of the shear layer (entrainment wave, actually, [6]) on the rear wall, a local high pressure area, a feedback compression wave, and a shock wave are formed near the trailing edge. At the same time, a local high pressure area is formed between the feedback compression wave and the trailing edge. When the feedback compression wave arrives at the leading edge like a tripper, the shear layer is disturbed.

As shown in Fig. 10b, the major 3-vortex structure is characteristic of the 2nd mode. The shedding vortices travel downstream, and change among different phases. In the case of Phase 1, the two rear vortices are separated, so that a separation line forms. The freestream fluid enters into the cavity along the separation line. The shedding vortices travel downstream in the case of Phase 2 and the two rear vortices extrude each other. The extrusion wave exists between the extruding vortices and the fluid in the cavity enters the freestream. The extrusion wave is a kind of compression wave. Thus, the feedback compression wave encounters the extrusion wave and they are constantly reinforced by each other (the feedback compression wave turns into a shock wave, possibly). Meanwhile, the instantaneous high pressure leads to the formation of a bow shock wave outside adapted to the shear layer shape, where the shear layer outflows along the extrusion wave. The reinforced extrusion wave and the feedback compression wave travel, together with the bow shock wave, above the shear layer; therefore, an “analogous sonic boom” phenomenon appears causing the violent noise in the cavity. To sum up, when the supersonic freestream spans an open cavity, on the one hand, the shear layer transport processes lead to the mass transfer inside and outside the

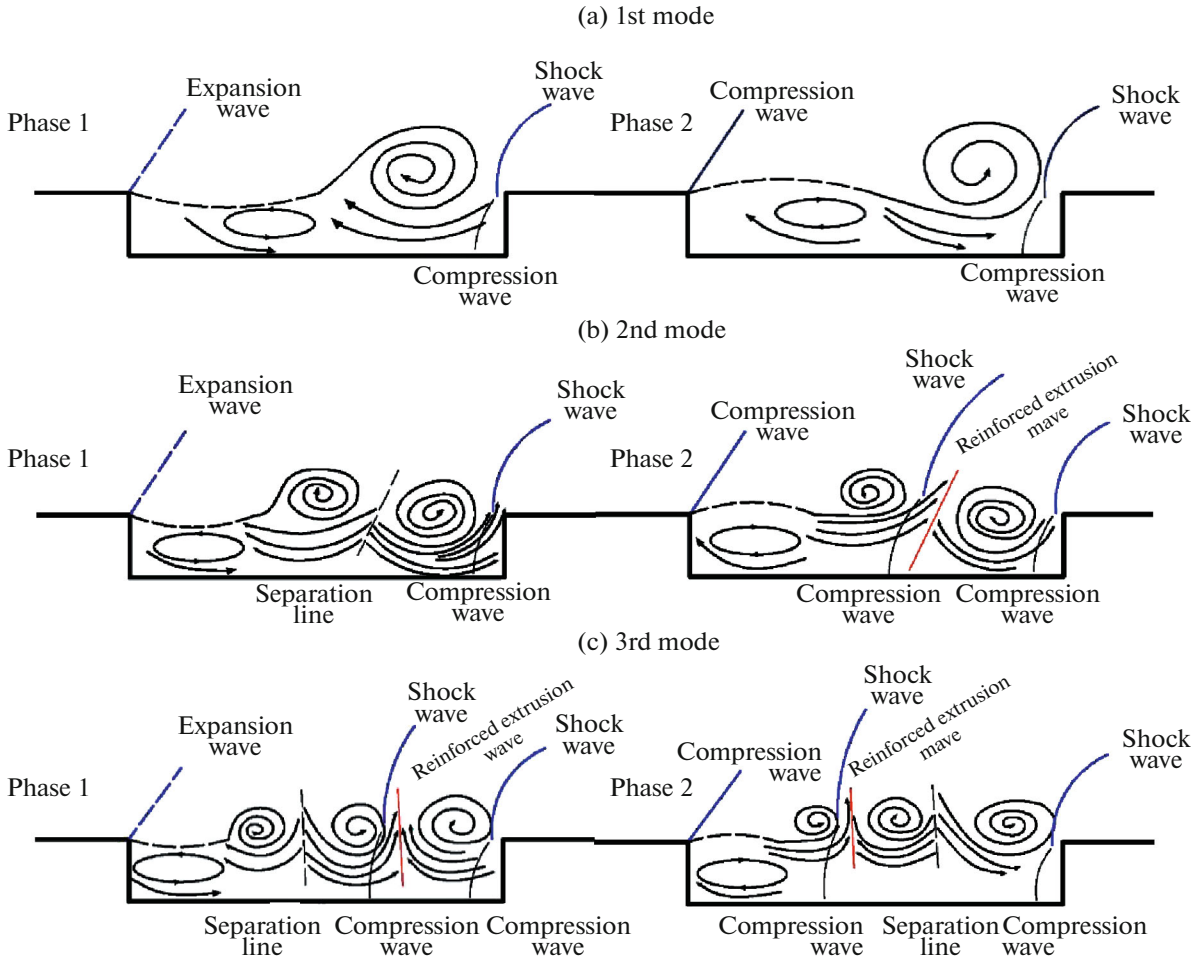

Fig. 10. Simplified DMD mode structures of the cavity flow dynamics.

cavity and, on the other hand, this mass transfer stimulates violent pressure fluctuations. As mentioned by Zhuang et al. [4] and Gautam et al. [28], the instable shear layer near the leading edge of the cavity "flaps" up and down. A compression wave is generated, when the shear layer flaps up, and an expansion wave is generated, when the shear layer flaps down.

Similarly to the 2nd mode, the major 4-vortex structure is characteristic of the 3rd mode (Fig. 10c). There are one separation line and one extrusion wave simultaneously. The violent noise is the result of the interaction between the feedback compression wave and the extrusion wave like in the case of the 2nd mode. Last but not the least, only if the feedback compression wave encounters the extrusion wave, moving shock waves are stimulated above the shear layer, and the structure of extrusion waves with different modes is discrete. Thus, it can be concluded that the feedback compression wave always exists in the feedback process but the bow shock waves are discontinuous.

SUMMARY

DES and DMD are used to calculate and analyze the cavity flow at the freestream Mach number of 1.19. The calculated SPL spectra and the OASPL on the cavity ceiling agree with Hamed's results. The results calculated in this study almost match with the frequencies estimated according to Heller's formula.

It is necessary to note that the coherent structures of the cavity flow dynamics with the specific frequencies were extracted by the DMD algorithm. The mean flow mode captures the time-mean flow structure. The Strouhal numbers corresponding to the dominant frequencies of the first three DMD modes are 0.2392, 0.6218, and 0.9878, respectively. The first three DMD modes extracted by the DMD algorithm are evolutive in the time domain and indicate two vortices, three vortices, and four vortices

spanning the length of the cavity, respectively. The vortices connected by the extrusion wave or the separation line translate downstream cyclically.

The comprehensive dynamics of the supersonic cavity are presented by the simplified mode structures. The feedback acoustic waves always exist in the cavity. Only when the acoustic wave travels to special locations, the shock waves can be stimulated outside the shear layer. The feedback acoustic wave is connected with the oblique shock wave. An extrusion wave is formed between two extruded vortices. When the feedback compression wave encounters the extrusion wave at a special location, they are invariably reinforced by each other and travel, together with the bow shock wave, above the shear layer; thus, an 'analogous sonic boom' phenomenon appears causing the violent noise in the cavity.

FUNDING

This work was supported by the Top-ranking Discipline (no. 15021540) Program of Chinese Liaoning province.

DECLARATION OF CONFLICTING INTERESTS

The Authors declare no potential conflicts of interest with respect to the research, authorship, and/or publication of this article.

REFERENCES

1. C. W. Rowley and D. R. Williams, "Dynamics and control of high-Reynolds-number flow over open cavities," Annu. Rev. Fluid Mech. **38**(1), 251–276 (2005).
2. J. E. Rossiter, "Wind tunnel experiments on the flow over rectangular cavities at subsonic and transonic speeds," RAE Techn. Rep. no. 3438 (1964).
3. C. K. W. Tam and P. W. Block, "On the tones and pressure oscillations induced by flow over rectangular cavities," J. Fluid Mech. **89**(2), 373–399 (1978).
4. N. Zhuang, F. S. Alvi, M. B. Alkislar, and C. Shih, "Supersonic cavity flows and theircControl," AIAA J. **44**(9), 2118–2128 (2006).
5. S. J. Moon, S. L. Gai, H. H. Kleine, and A. J. Neely, "Supersonic flow over straight shallow cavities including leading and trailing modifications," AIAA-2010-4687 (2010).
6. R. F. Schmit, L. T. F. Semmelmayer, and L. T. M. Haverkamp, "Fourier analysis of high speed shadowgraph images around a Mach 1.5 cavity flow field," AIAA-2011-3961 (2011).
7. H. Wang, P. Li, M. Sun, and J. Wei, "Entrainment characteristics of cavity shear layers in supersonic flows," Acta Astronautica **137**, 214–221 (2017).
8. D. G. Yang, J. Q. Li, and Z. L. Fan, "Aerodynamic characteristics of transonic and supersonic flow over rectangular cavities," Flow, Turbulence, and Combustion **84**(4), 639–652 (2006).
9. R. F. Schmit, J. E. Grove, and A. Ahmed, "Examining passive flow control using high speed shadowgraph images in a Mach 1.5 cavity flow field," Intern. J. Flow Control **5**(3), 153–186 (2013).
10. T. Colonius, "An overview of simulation, modeling, and active control of flow/acoustic resonance in open cavities," AIAA-2001-0076 (2001).
11. C. W. Rowley, T Colonius, and R. M. Murray, "Dynamical models for control of cavity oscillations," AIAA-2001-2126 (2001).
12. P. J. Schmid, "Dynamic mode decomposition of numerical and experimental data," J. Fluid Mech. **56**, 5–28 (2010).
13. G. H. Gunaratne, D. G. Talley, J. R. Gord, and S. Roy, "Dynamic mode decomposition based analysis of shear coaxial jets with and without transverse acoustic driving," J. Fluid Mech. **790**, 5–32 (2016).
14. T. Sayadi, P. J. Schmid, F. Richecoeur, and D. Durox, "Parametrized data-driven decomposition for bifurcation analysis, with application to thermo-acoustically unstable systems," Phys. Fluids **27**(3), 037102-1013 (2015).
15. C. Pan, D. Yu, and J. Wang, "Dynamical mode decomposition of gurney flap wake flow," Theor. Appl. Mech. Letters **1**(1), 42–46 (2011).
16. A. Seena and H. J. Sung, "Dynamic mode decomposition of turbulent cavity flows for self-sustained oscillations," Intern. J. Heat Fluid Flow **32**, 1098–1110 (2011).
17. A. Wynn, D. S. Pearson, B. Ganapathisubramani, and P. J. Goulart, "Optimal mode decomposition for unsteady flows," J. Fluid Mech. **733**(10), 473–503 (2013).
18. M. Jovanovic and P. Schmid, "Sparsity-promoting dynamic mode decomposition," Phys. Fluids **26**(2), 561–571 (2013).

19. M. S. Hemati, C. W. Rowley, E. A. Deem, and L. N. Cattafesta, "De-biasing the dynamic mode decomposition for applied Koopman spectral analysis," J. Nonlinear Sci. **25**(6), 1–40 (2015).
20. M. S. Gritskevich, A. V. Garbaruk, J. Schutze, and F. R. Menter, "Development of DDES and IDDES formulations for the $k-\omega$ shear stress transport model," Flow, Turbulence and Combustion **88**(3), 431–449 (2012).
21. A. Hamed, D. Basu, and K. Das, "Detached eddy simulations of supersonic flow over cavity," AIAA-2003-549 (2010).
22. R. G. Abdrashitov, E. Y. Arkhireeva, B. N. Dan'Kov, V. S. Korotaev, A. P. Kosenko, O. Yu. Popov, O. K. Strel'tsov, and I. B. Chuchkalov, "Numerical and experimental investigation of the means for reducing the aeroacoustic loads in an extended rectangular cavity at subsonic and transonic freestream velocities," Fluid Dynamics **52**(2), 239–252 (2017).
23. B. H. K. Lee, "Pressure waves generated at the downstream corner of a rectangular cavity." J. Aircraft **47**(3), 1064–1066 (2010).
24. J. C. R. Hunt, A. A. Wray, and P. Moin, "Eddies stream and convergence zones in turbulent flows," Center for Turbulence Research, **CTR-S88**, 193–209 (1988).
25. B. N. Dan'kov, A. P. Duben', and T. K. Kozubskaya, "Numerical modeling of the self-oscillation onset near a three-dimensional backward-facing step in a transonic flow," Fluid Dynamics **51**(4), 534–543 (2016).
26. H. Heller and J. Delfs, "Cavity pressure oscillations: the generating mechanism visualized," J. Sound Vibr. **45**, 248–252 (1996).
27. C. W. Rowley, I. Mezić, and S. Bagheri, "Spectral analysis of nonlinear flows," J. Fluid Mech. **641**, 115–127 (2009).
28. T. Gautam, G. Lovejeet, and A. Vaidyanathan, "Experimental study of supersonic flow over cavity with aft wall offset and cavity floor injection," Aerospace Science & Technology **70**, 211–232 (2017).